

From Turing patterns to chimera states in the 2D Brusselator model

A. Provata^{a)}

Institute of Nanoscience and Nanotechnology, National Center for Scientific Research “Demokritos”, 15341 Athens, Greece

(Dated: 5 December 2022)

The Brusselator has been used as a prototype model for autocatalytic reactions, and in particular for the Belousov-Zhabotinsky reaction. When coupled at the diffusive limit, the Brusselator undergoes a Turing bifurcation resulting in the formation of classical Turing patterns, such as spots, stripes and spirals in 2 spatial dimensions. In the present study we use generic nonlocally coupled Brusselators and show that in the limit of the coupling range $R \rightarrow 1$ (diffusive limit), the classical Turing patterns are recovered, while for intermediate coupling ranges and appropriate parameter values chimera states are produced. This study demonstrates how the parameters of a typical nonlinear oscillator can be tuned so that the coupled system passes from spatially stable Turing structures to dynamical spatiotemporal chimera states.

Oscillating reactions, also known as chemical clocks, have been studied intensively in the past, with notable examples the Bray-Liebhafsky reaction (1921), the Belousov-Zhabotinsky reaction (1958), the Briggs-Rauscher reaction (1972) and the Chlorite-Iodide-Malonic Acid (CIMA) reaction (1990). They are characterized by periodical color changing or periodic gas emissions and this periodic activity was earlier considered as a contradiction to common sense. The explanation of the mechanisms behind the unexpected concentration oscillations was proposed in the 1970’s, and relies on the nonlinear nature of the interactions between the species, which give rise to a limit cycle following a Hopf bifurcation scenario¹. The same nonlinear mechanisms are responsible for the emergence of spectacular Turing patterns when spatial diffusion is taken into account, as demonstrated by Alan Turing in his 1952 seminal paper². In the present study we quest the existence of a different unexpected spatiotemporal effect, the chimera states, which are mainly observed in nonlinear reactive dynamics at intermediate coupling ranges, whereas the Turing patterns emerge at the limit of local diffusive coupling. To that purpose, we study the generic Brusselator model^{3,4}, which was proposed as a reduction of the complex chemical mechanism representing the Belousov-Zhabotinsky reaction. For this model we show, in a unifying description, that by appropriate choice of the parameter values and coupling ranges we can pass from the spatial Turing patterns to the oscillating spatiotemporal chimera states. In the simulations coupled Brusselators linked in 2D torus geometry are employed, where both Turing patterns and chimera states demonstrate spectacular formations.

the same dynamical system. For this reason we use a typical nonlinear dynamical system with minimal number of variables (two), the Brusselator, constructed specifically to model the complex spatiotemporal organization of the Belousov-Zhabotinsky reaction (see⁵ and references therein). For this model, we numerically demonstrate that it is possible to drive the system from spatial Turing pattern to spatiotemporal oscillating chimera states by controlling the range of the diffusion from classical (local) diffusion to intermediate range (nonlocal) diffusion with appropriate choice of the reaction rates (parameters).

Turing patterns were first predicted in 1952 by Alan Turing in a set of nonlinear PDEs describing a hypothetical chemical reaction, which involved autocatalytic steps and species diffusion². Experimentally, these states were observed in several reactive systems beyond the Belousov-Zhabotinsky, such as the Bray-Liebhafsky, the Briggs-Rauscher and the Chlorite-Iodide-Malonic Acid (CIMA) reactions^{1,6-10}. Regarding the numerical evidence of Turing patterns, until the late 1980’s it was generally admitted in the literature that “Albeit their prediction by Turing, chemical periodic stationary patterns under far from equilibrium conditions, ... have not yet been observed in a clear-cut way”¹¹. Nevertheless, a few years later, in the early 1990s, numerical simulations corroborated the experimental findings and the theoretical predictions. Turing patterns were then reported using a number of models, including the Brusselator¹²⁻¹⁴, the two- and three-variable Oregonator models^{6,15-19} and the two-variable Zhabotinsky-Buchholtz-Kiyatkin-Epstein (ZBKE) model^{20,21}.

On the other end, chimera states have recently been the subject of intensive studies since their first discovery by Kuramoto and Battogtokh in 2002^{22,23}. The term “chimera”, proposed by Abrams and Strogatz²⁴, dominated two years after their first introduction and refers precisely to a hybrid state. Indeed, in networks composed of identical and identically linked oscillators, as Kuramoto and Battogtokh demonstrated, a hybrid state is often established which consists of stable, coexisting, coherent and incoherent domains. Originally, the chimera states were observed under nonlocal network connectivity, but later works using local connectivity and non-identical oscillators have also reported emerging chimera states. In the first studies, the phase oscillator was used as the dynamics on the network nodes²⁵⁻²⁷, while most recent

I. INTRODUCTION

The motivation of the present study is to describe, in a unifying way, the emergence of spatial structures and spatiotemporal patterns in different regions of the parameter space in

^{a)}Electronic mail: a.provata@inn.demokritos.gr

studies have demonstrated the presence of chimera states in a number of nonlinear oscillators, such as the Hodgkin-Huxley (HH)²⁸, the FitzHugh-Nagumo (FHN)^{29–33}, the Hindmarsh-Rose³⁴, the Van der Pol³⁵, the Stuart-Landau^{36–38}, the Leaky Integrate-and-Fire (LIF)^{39–41} and other oscillator networks. In the above studies the presence of chimera (multichimera) states were reported with one (many) coherent and incoherent domains. The patterns and multiplicity of the chimeras depend on the parameters governing both the nodal dynamics and the network coupling.

The role that the network architecture plays in the form of the chimera states has also been the subject of recent intense investigations. Most of the studies cited above were performed in a 1D connectivity with periodic boundary condition (K-ring connectivity). Considerably fewer studies concern connectivities in higher spatial dimensions. Studies in 2D-square (torus) connectivity have revealed coherent (and incoherent) domains of circular disc shapes, stripes, spots, scroll waves etc^{31,42–44}. Similar studies in 3D-cubic (hypertorus) connectivity produce coherent and incoherent domains of higher complexity, such as spheres, cylinders, layers and combinations of these^{42,44–48}.

Almost one decade after the first theoretical prediction of chimera states, experimental evidence of these states were reported in a number of mechanical, physical and chemical systems consisting of interacting oscillatory units. Some examples reported in the literature include chimeras in experiments in optical systems⁴⁹, in electronic circuits⁵⁰, in mechanics (systems of coupled mechanical oscillators)^{51–54}, in biomedicine^{55–58}, and in reaction diffusion systems^{59–61}. Beyond experimental findings in the laboratory, chimera states have been associated with the uni-hemispheric sleep in mammals and birds^{62–64}, with the onset of epileptic seizures^{56,57} and other biomedical conditions^{48,65–67}. For reviews on the recent theoretical and experimental developments in the field of chimera states, see references^{68–74}.

Regarding the emergence of chimera states in reaction-diffusion systems, the first such reports date as early as 2012. In particular, photochemically coupled Belousov-Zhabotinsky micro-oscillators have been shown to produce complex synchronization phenomena, such as spiral wave chimeras, spiral wave core splitting and phase cluster states^{21,59,75–78}. Numerical simulations using the dimensionless Zhabotinsky-Buchholtz-Kiyatkin-Epstein (ZBKE) model with a time delay in the coupling between the oscillators corroborate the experimental findings^{76–78}. These studies indicate that chimera states are not only theoretical predictions but are realized in chemical experimental setups. Additional evidence of chimera states in reaction-diffusion systems has been reported by the present author and collaborators in a different numerical study drawing from population dynamics and reactive systems in cyclic reactions⁷⁹. In this study, the Lattice Limit Cycle (LLC) model was considered with 4-th order nonlinearities. Nonlinearly coupled LLCs were shown to produce chimera states in the spiking regime, when the bifurcation parameter increases away from the Hopf bifurcation. More recent studies investigating the presence of Turing patterns and chimera states in networks of nonlinear oscillators have been

reported in the literature for the phase oscillator⁸⁰ and for coupled SQUID models⁸¹.

As earlier stated, in the present study we consider a well known reaction diffusion scheme, the Brusselator, proposed as a minimal prototype scheme for demonstrating the effects of nonlinear interactions in chemistry. Its minimal dynamics involves two interacting variables with 3rd order nonlinearities and an autocatalytic step. Numerous studies in the past have shown that this model gives rise to interesting Turing patterns in 1D, 2D and 3D spatial geometries, when normal diffusion in the form of nearest neighbor interactions is included in the dynamics and the parameter values are chosen in the Turing bifurcation regime^{12–14,82–86}. In the sequel, we extend gradually the range of interactions, going from nearest neighbors (normal diffusion) to nonlocal, intermediate ranges where the chimera states prevail. In parallel, we determine the reaction rates and parameter ranges which trigger the appearance of complex synchronization phenomena and chimera states in two spatial dimensions.

The organization of the study is as follows: In the next section, II, we introduce the uncoupled (II A) and the coupled (II B) Brusselator model and discuss its mean field dynamics and the conditions and parameters for the Hopf and the Turing bifurcations. At the end of the same section we introduce some quantitative measures appropriate for the description of Turing patterns and chimera states. In section III, we show that by taking the diffusing limit in the coupling range we obtain Turing structures of different morphologies. In section IV, we increase the coupling range and for appropriate parameter values (after Hopf bifurcation) we demonstrate the emergence of chimera states. By scanning the coupling range and coupling angle parameters we determine the region in the parameter space where the chimera states dominate. In section V, the nature of Turing and chimera patterns are discussed using the Fourier transforms of the simulated evolution of the systems' variables. In the concluding section, we recapitulate our main results and propose open problems.

II. THE MODEL

In this section we first present the ODEs of the uncoupled Brusselator model and discuss, in brief, the Hopf bifurcation scenario giving rise to a limit cycle. Next, we present the nonlocally coupled Brusselator network and discuss the emergence of a Turing bifurcation at the limit of local coupling. In the last part of this section, we introduce some quantitative indices for quantifying the spatial and temporal properties of the system.

A. The uncoupled Brusselator Model

As discussed in the Introduction, the Brusselator model was introduced in late 1960's by R. Lefever, G. Nicolis and I. Prigogine as a minimal, two-variable, autocatalytic model producing all spatiotemporal complexity of the Belousov-Zhabotinsky oscillatory reaction^{3,4}. It consists of two ODEs

of 3rd order, with two variables, X and Y , and two control parameters, A and B , as follows:

$$\frac{dX}{dt} = A - (B+1)X + X^2Y \quad (1a)$$

$$\frac{dY}{dt} = BX - X^2Y. \quad (1b)$$

In Eqs. (1), the variables X and Y take positive values since they were first constructed to represent chemical species concentrations, while the parameters A and B represent the initial product concentrations and remain constant (considered as sources).

The Brusselator model, Eqs. (1), has a single fixed point, X_s ,

$$(X_s, Y_s) = (A, B/A). \quad (2)$$

Stability analysis around (X_s, Y_s) reveals that this fixed point changes its asymptotic stability when the parameter B attains its critical value B_c :

$$B_c = A^2 + 1. \quad (3)$$

Namely, for $B < B_c = A^2 + 1$, (X_s, Y_s) is a stable node or stable focus and the phase space trajectories are attracted to the fixed point. At $B = B_c$ the dynamics around the fixed point changes from asymptotic stability to instability and beyond this point a limit cycle is created⁵. Because limit cycles are stable oscillators under reasonable perturbations, they are prerequisites for the emergence of the complex synchronized states, chimera states, when many limit cycles are coupled in networks. For this reason, in section IV the parameter values $A = 1.0$ and $B = 2.5 - 3.5$ will be used (such that $B > A^2 + 1$), when the

network composed by Brusselator units will be tuned to produce chimera states.

On the other hand, in the Brusselator model the Turing structures are produced away from the regime of limit cycles and under the Turing bifurcation conditions, where the coupling terms need to be taken into account. For this reason, the discussion on the precise Brusselator parameter values which lead to the emergence of Turing structures is postponed till section III, after the coupling terms have been included.

B. The coupled Brusselator Model

In this section, spatial coupling is introduced between units in 2D, square lattice geometry. Earlier studies have discovered spectacular Turing patterns in 2D, such as dots and stripes, and the aim of the present work is to clarify the different parameter domains in the 2D Brusselator network where the Turing patterns and the chimera states reside. On the square lattice network containing $N \times N$ units, the Brusselator located at position coordinates (i, j) is described by the time dependent variables X_{ij} and Y_{ij} . The communication between the Brusselators is achieved by the coupling matrix C whose elements, $c_{ij:kl}$, represent the strength of the link between Brusselators at positions (i, j) and (k, l) on the network, with $i, j, k, l \leq N$. Recent investigations of synchronization phenomena on complex networks have shown that coupling matrices with strong cross-coupling terms (w_{XY} , w_{YX}) and both excitatory (positive) and inhibitory (negative) terms are necessary (but not sufficient) for partial synchronization in the form of chimera states^{29,72}. Under these conditions, the nonlocally coupled Brusselator dynamics on the 2D square lattice is governed by the following equations:

$$\frac{dX_{ij}}{dt} = A - (B+1)X_{ij} + X_{ij}^2Y_{ij} + \sum_{(k,l)} c_{kl:ij} [w_{XX}(X_{kl} - X_{ij}) + w_{XY}(Y_{kl} - Y_{ij})] \quad (4a)$$

$$\frac{dY_{ij}}{dt} = BX_{ij} - X_{ij}^2Y_{ij} + \sum_{(k,l)} c_{kl:ij} [w_{YX}(X_{kl} - X_{ij}) + w_{YY}(Y_{kl} - Y_{ij})] \quad (4b)$$

In Eqs. 4, we implicitly assume that all Brusselators are identical since they have the same parameters A and B .

The coupling matrix C is limited by the range R and

strength σ of the nonlocal interactions. The elements $c_{ij:kl}$ representing the interactions between Brusselators at positions (i, j) and (k, l) have the form:

$$c_{ij:kl} = \begin{cases} \frac{\sigma}{(2R+1)^2 - 1}, & \text{when } i-R \leq k \leq i+R, \quad j-R \leq l \leq j+R \\ 0, & \text{otherwise.} \end{cases} \quad (5)$$

Namely, the Brusselator at position (i, j) is coupled with all other elements located only within a rectangle of size

$(2R+1) \times (2R+1)$, whose center is at position (i, j) . Each nonzero link carries constant weight (coupling strength) σ ,

while the overall contribution is normalized by the total number of nonzero links, which is $(2R + 1)^2 - 1$. In Eqs. (4) and (5), periodic boundary conditions on the torus are considered and, therefore, all indices i, j, k, l , are taken mod N .

Apart for the coupling matrix C between the nodes of the network, a rotational matrix, W , is introduced to account for the cross-coupling terms. W contains both diagonal coupling, in the form (w_{XX}, w_{YY}) and cross coupling (w_{XY}, w_{YX}) and is parameterized by a single parameter φ , which is close to $\pi/2$ if cross-coupling is dominant²⁹. This coupling phase φ is similar to the phase-lag parameter α of the paradigmatic Kuramoto phase oscillator model, which is widely used to generically describe coupled oscillator networks. The coupling phase is necessary for the development of nontrivial partial synchronization patterns, as has been shown for the Kuramoto model⁸⁷ and for the FHN model²⁹. This rotational matrix W is also used in Refs.^{30,31,64,88} and has the form:

$$W = \begin{pmatrix} w_{XX} & w_{XY} \\ w_{YX} & w_{YY} \end{pmatrix} = \begin{pmatrix} \cos \varphi & \sin \varphi \\ -\sin \varphi & \cos \varphi \end{pmatrix}. \quad (6)$$

In the present study different values of the coupling range R and the coupling phase $0 \leq \varphi \leq 2\pi$ are examined to determine the domains in the (φ, R) parameter intervals where the Turing patterns or the chimera states dominate.

C. Quantitative measures

The synchrony/asynchrony in the coupled Brusselator system can be verified using the mean phase velocity profile, as in most studies where many oscillators are interlinked. The mean phase velocity ω_{ij} accounts for the average number of cycles that oscillator at position (i, j) has performed in the time unit^{30,41}. Let us call Q_{ij} the number of complete cycles that oscillator (i, j) has performed during a certain time interval ΔT . Then ω_{ij} is defined as:

$$\omega_{ij} = 2\pi \frac{Q_{ij}}{\Delta T} = 2\pi f_{ij}, \quad (7)$$

where f_{ij} is the frequency of the oscillator at position (i, j) . Because the definitions of frequency and mean phase velocity differ by just a factor of 2π , in the following the two expressions (“frequency” and “mean phase velocity”) are used interchangeably.

Chimera states are characterized by a distribution of frequencies, while the coherent states are characterized by a single, common frequency. Full incoherence may also be characterized by a single, common frequency, in some cases. Let us denote by $\omega_{\min} = \min\{\omega_{ij}\}$, $1 \leq i, j \leq N$, the minimum mean phase velocity recorded in the Brusselator network. Similarly, $\omega_{\max} = \max\{\omega_{ij}\}$, $1 \leq i, j \leq N$, is the maximum mean phase velocity observed. The difference

$$\Delta\omega = \omega_{\max} - \omega_{\min}, \quad (8)$$

is a measure of the extent of the mean phase velocity distribution in the system. We may assume that if $\Delta\omega > 2 * \pi / \Delta T$,

then the difference of the mean phase velocity between nodes can be considered significant and may be an indication of the establishment of a chimera state in the network. If $\Delta\omega < 2 * \pi / \Delta T$, this might be considered as a one-cycle over- or under-estimation and can be regarded as the error threshold.

The Kuramoto order parameter is another measure often used to quantify coherence/incoherence in the system^{22,89}. Let us denote θ_{ij} the instantaneous phase of Brusselator at position (i, j) , which is defined as $\theta_{ij} = \arctan[Y_{ij}/X_{ij}]$. The Kuramoto order parameter Z is defined globally, over the entire system as:

$$Z = \frac{1}{N^2} \left| \sum_{i,j} e^{+i\theta_{ij}} \right|. \quad (9)$$

In Eq. (9), if the system is synchronous and all phases are identical, then $Z = 1$. If all phases are random as in the asynchronous state, the various phases in the sum of Eq. (9) cancel out and $Z = 0$. For intermediate cases, where synchronous and asynchronous regions are present, $0 < Z < 1$, and this is the domain where chimera states can be observed. On the other hand, even in cases that the oscillators in the network have identical mean phase velocities but they operate under constant phase lags, they can be mistakenly considered as chimera states, because $Z < 1$. Therefore, both measures $\Delta\omega > 0$ and $0 < Z < 1$ are necessary to quantify synchronization in networks of coupled elements.

Other measures such as the spatial and/or temporal Fourier spectra can be used to further verify the spatial and/or temporal order of the network nodes, respectively.

III. TURING STRUCTURES IN 2D

Classical Turing structures are obtained when a nonlinear reactive system (the Brusselator in the present case) is subjected to interactions in the form of diffusion. The diffusion terms which are added to the original Brusselator model, Eqs. (1), involve the Laplacian operator and have the form $D_X \nabla^2 X$ for Eq. (1a) and $D_Y \nabla^2 Y$ for Eq. (1b). The parameters D_X and D_Y represent the diffusion coefficients and Eqs. (1) then become:

$$\frac{dX}{dt} = A - (B + 1)X + X^2Y + D_X \nabla^2 X \quad (10a)$$

$$\frac{dY}{dt} = BX - X^2Y + D_Y \nabla^2 Y. \quad (10b)$$

The study of these equations demonstrates that the fixed point (X_s, Y_s) undergoes a Turing bifurcation at a critical value B_c^T of the parameter B , such that^{5,12,14}:

$$B_c^T = (1 + \eta A)^2, \quad \eta = \left(\frac{D_X}{D_Y} \right)^{1/2} < (1 + A^2)^{1/2} - 1. \quad (11)$$

In addition, the discretization in space of the Laplacian operator retains only interactions with the first neighbors, and

Eqs. (10) reduce to (see Appendix A for the derivation):

$$\frac{dX_{ij}}{dt} = A - (B+1)X_{ij} + X_{ij}^2 Y_{ij} + \frac{D_X}{h^2} \sum_{\{k,l\}} [X_{kl} - X_{ij}] \quad (12a)$$

$$\frac{dY_{ij}}{dt} = BX_{ij} - X_{ij}^2 Y_{ij} + \frac{D_Y}{h^2} \sum_{\{k,l\}} [Y_{kl} - 2Y_{ij}]. \quad (12b)$$

Here the indices vary as $i-1 \leq k \leq i+1$ and $j-1 \leq l \leq j+1$, (i.e., the coupling range $R=1$) and h denotes the lattice constant. Equations (12) are of the same form as Eqs. (4), with the following parameter identifications

- a) $c_{ij;kl} w_{XX} = D_X/h^2$,
- b) $c_{ij;kl} w_{YY} = D_Y/h^2$,
- c) $w_{XY} = w_{YX} = 0$ and
- d) $R = 1$.

With these parameter identifications and under restrictions Eq. (11), the generic coupled Brusselator system, Eqs. (4), may produce Turing patterns as shown in Fig. 1.

For the simulations in Fig. 1 all systems started with the same random initial conditions. As working parameter set, generic values were used (obeying conditions Eq. (11)), namely, $A = 4.5$, $D_X = 7.0$, $D_Y = 56.0$, $w_{XY} = w_{YX} = 0$. The constant $h = 1$ as it is representing the lattice constant (absolute distance between successive nodes), as described in the Appendix A. On the left panels of Fig. 1 the parameter B takes the value $B = 6.75$, while on the right ones $B = 8.0$. All systems were integrated for 1500 Time Units (TUs), i.e., for 1500×10^3 integration steps. The Turing patterns stabilized between 300 and 400 TUs and remained stable thereafter.

Different values of coupling range are used, $R = 1$ at the top row, $R = 2$ in the middle row and $R = 3$ in the last row, to demonstrate how the Turing patterns dissolve as the coupling range increases from local (nearest neighbor) coupling to nonlocal coupling. Note that the local coupling $R = 1$ corresponds directly to the diffusion operator, while for $R > 1$ we step away from the dominance of the diffusion coefficient and the Turing bifurcation analysis is no longer valid.

In Fig. 1 panel (a1), stable Turing spot patterns are recorded for $B = 6.75$ and $R = 1$ and all other parameters as in the working parameter set, described in the previous paragraph and also provided in the legend of Fig. 1. Note that the size of spots increases with D_X and D_Y (not shown). In panel (a2) stable stripe patterns are recorded, for $B = 8.0$ and $R = 1$. In both panels (a1) and (a2) the parameters obey conditions Eqs. (11) while the coupling range $R = 1$, attains the limit of diffusion on lattice¹²⁻¹⁴.

The criterion on the coupling range is relaxed in the middle row of Fig. 1. Here the coupling range is increased to the value $R = 2$ and now the size of the spots and stripes increases leading to fewer spots of larger radius in Fig. 1(b1) and fewer stripes of larger width in Fig. 1(b2). Increasing further the coupling range to $R = 3$ in the last row of Fig. 1, we note that the size of the spots increases further and they merge into strips, see Fig. 1(c1). Note also that the range of

the X -variable decreases inversely with R and the system tends to the pure homogeneous state as R increases. Similarly, in Fig. 1(c2) the width of the stripes increases with R and even fewer stripes are formed, leading again to the homogeneous state as R increases further.

The reason for increasing of the size of the patterns (spots, stripes) with the coupling range R can be intuitively understood, because for larger R each node connects to a larger number of neighbors and therefore the elements can adjust their variables at larger distances/areas. A similar effect can be also seen in the next section, where the chimera states synchronize at larger distances/areas, as the coupling range increases.

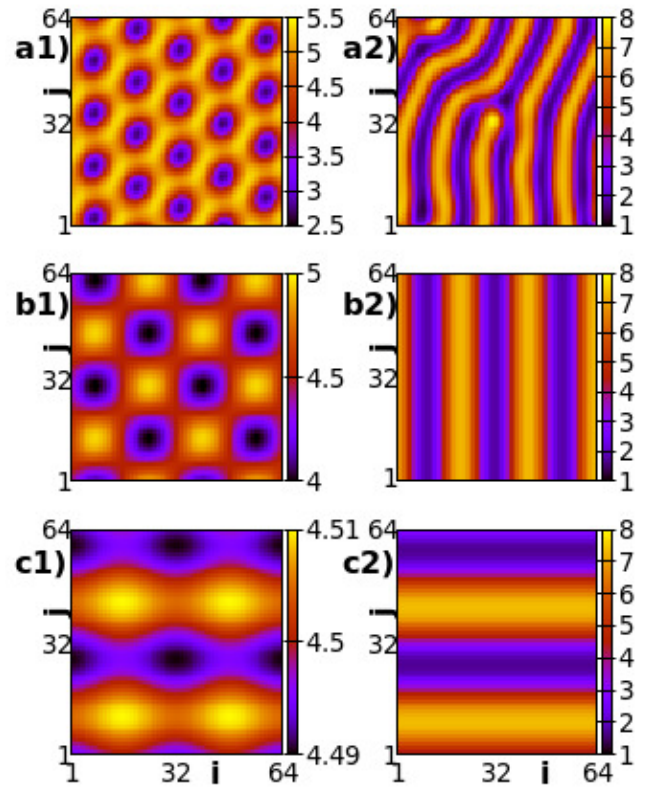


FIG. 1. Color-coded stable snapshots (X -variable profiles), Turing patterns, of the coupled Brusselator network. **a1)** Multiple spots for $B = 6.75$ and $R = 1$, **a2)** multiple stripes, for $B = 8$ and $R = 1$, **b1)** Multiple spots for $B = 6.75$ and $R = 2$, **b2)** multiple stripes, for $B = 8$ and $R = 2$, **c1)** Multiple spots for $B = 6.75$ and $R = 3$ and **c2)** multiple stripes, for $B = 8$ and $R = 3$. For all integrations Eqs. (4) and (5) were used, with the following parameters: $N = 64$, $A = 4.5$, $D_X = 7.0$, $D_Y = 56$, $w_{XY} = w_{YX} = 0$, $h = 1$, $\sigma = 1$ with the integration constant $dt = 0.001$. Images are recorded at 640 TUs. Simulations start from random initial conditions with periodic boundary conditions. Two related videos are presented in the Supplementary Material (Multimedia view corresponding to images Fig. 1(a1) (movie_fig1a1_aa4.5_bb6.75_du7.0_dv56.0_dt0.001.mp4) and Fig. 1(a2) (movie_fig1a2_aa4.5_bb8.00_du7.0_dv56.0_dt0.001.mp4)).

Specific features of the patterns in Fig. 1 can be extracted

R	Spots		Stripes	
	Amplitude	Wavelength	Amplitude	Wavelength
1	1.03	15.84	2.7395(h)	12.66(h)
2	0.32	31.79	2.83(h)	21.07(h)
3	0.01	31.56	2.88(v)	31.62(v)
4	0.58	63.01	2.97(h)	63.10(h)
5	7×10^{-8}	63.01	2.44(h)	63.10(h)

TABLE I. The amplitude and wavelength of the spots and stripes patterns in Fig. 1 for different values of the coupling range R . The values related to the spot pattern are averages over the x - and y -spatial directions. The notation (h) or (v) in the stripes pattern denote that the amplitude and wavelength were computed in the horizontal or vertical direction, respectively. The parameter values are as in Fig. 1.

via the Fourier transform, and the spatial wave length can be considered as a function of the coupling radius. The results are shown in Table I.

In Table I, on the 2nd and 3rd columns, the amplitudes and wavelengths of the spot pattern are presented for different R values, as corresponding to Fig. 1 (left column). They were computed as averages over the amplitudes and wavelengths in the x - and y - directions. It is easy to understand that as R increases the wavelength increases and for $R = 4$ and 5 one wavelength covers the entire system. In addition, for $R = 4$ there is a non-negligible mode amplitude ($= 0.58$), while for $R = 5$ the amplitude tends to zero, indicating that the system has reached the homogeneous steady state.

Similar conclusions are reached for the stripe pattern. Depending on the orientation of the stripes, the amplitudes and wavelengths recorded in the 4th and 5th columns of the Table I were computed either in the horizontal (x -) direction and are denoted by the letter (h) or in the vertical (y -) direction and are denoted by the letter (v). Here also, as R increases from 1 to 2 and to 3, the wavelength doubles each time. For $R = 4$, one wavelength covers the entire system with non-negligible amplitude ($= 2.97$). As the coupling range increases further to $R = 5$, still one wavelength covers the entire system, but the amplitude of the spatial oscillations decreases ($= 2.44$). Therefore, the amplitude of the patterns decreases with R , leading again to the homogeneous steady state for large R -values.

The results of Table I and Fig. 1 highlight the special characteristics of the Turing patterns. They are best observed at the diffusion limit, which corresponds to $R = 1$ in the discrete lattice version of the equations, and they dissipate as R increases leading to homogeneous steady states. As we will see in the next section, this is not the case for the chimera states. Not only the chimeras are observed in the parameter regions where limit cycles are supported but they also appear away from the diffusing limit, at intermediate coupling ranges.

We would like to stress here that we do not go into a deep study of the pattern formation of the Brusselator model, this has been done extensively elsewhere^{12–14,82–86}. We only highlight the dissolution of the Turing patterns as the coupling range increases, in contradistinction with the behavior of chimera states, which are not supported at the diffusing limit,

but only at intermediate coupling ranges (provided that all oscillators are identical).

IV. CHIMERA STATES IN 2D

The same model, Eqs. (4) with connectivities as in (5) and (6), for appropriate parameter values and intermediate coupling ranges can lead to oscillatory steady states with coexisting variable frequencies on the network, known as chimera states. To demonstrate this, we integrate numerically the aforementioned equations, using the following working parameter set: $A = 1.0$, $B = 2.9$ to place the uncoupled Brusselator in

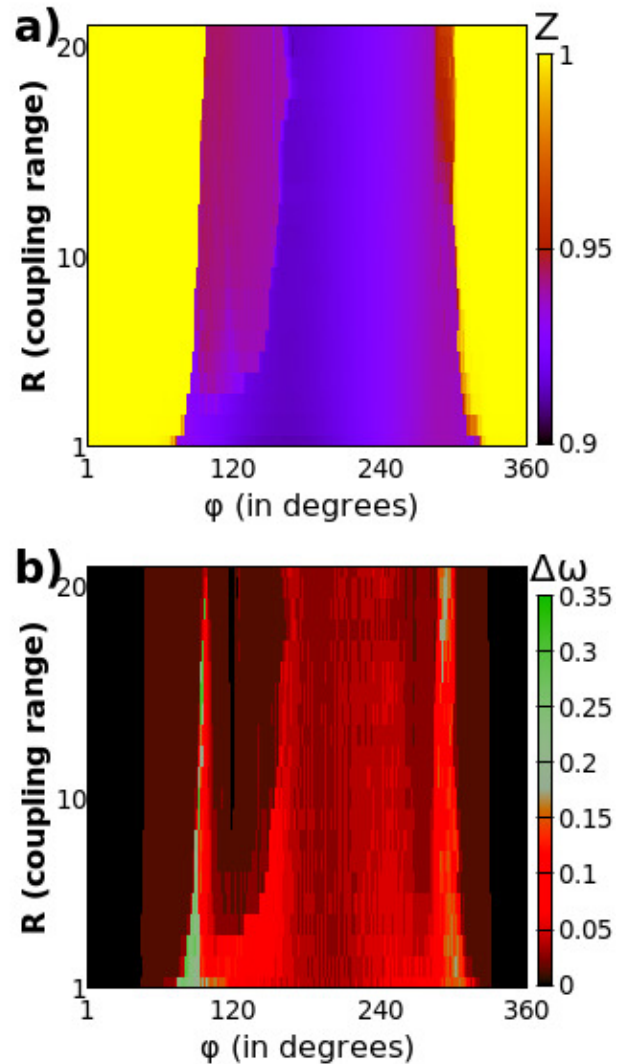


FIG. 2. Color-coded values of a) the Kuramoto order parameter Z and b) the frequency deviation in the system, $\Delta\omega$, as a function of the coupling range R and the coupling angle ϕ . Other parameters for the Brusselator model are $A = 1.0$, $B = 2.9$. Integration parameters are set to $dt = 0.010$, $D_x = D_y = 1$. The network is a 2D square lattice with periodic boundary conditions and size $N \times N = 64 \times 64$. All simulations start from the same random initial conditions.

the parameter domain where limit cycles are observed, see section II A. The integration parameters are set to $dt = 0.010$, $D_X = D_Y = 1$ and the 2D network consists of a square lattice composed by $N \times N = 64 \times 64$ elements, with periodic boundary conditions (same as in the previous section, III, where the Turing patterns are produced). The coupling strength σ is set to unity. To explore the presence of chimera states in the Brusselator network, the coupling range R and coupling angle φ were varied in the ranges, $1 \leq R \leq 21$ and $0 \leq \varphi < 2\pi$ (or $0 \leq \varphi < 360$ in degrees).

As discussed in section II C, the presence of chimera states is characterized by values of the Kuramoto order parameter Z such that $0 < Z < 1$ and $\Delta\omega > 0$. In Fig. 2a, we present the values of Z in a color-coded map, as a function of R and φ . We note that chimera states can be sought in the regions that the Z -values take dark colors and away from the yellow regions. Similarly, in Fig. 2b, we present the values of $\Delta\omega$ in a color-coded map. In the $\Delta\omega$ map, there is evidence of chimera presence in the red and green regions which support high divergence of local frequencies in the system.

Both images, Fig. 2a and b, give compatible information as far as the parameter regions where chimera states are realizable. Namely, for small values of $\varphi < 90^\circ$ and all values of R chimera states are not possible: the Kuramoto order parameter $Z \sim 1$, the frequency distribution $\Delta\omega \sim 0$ then coherence reigns in the system. Similarly, chimera states are not promoted for high values of $\varphi > 280^\circ$. This is in agreement with previous studies of other models (such as the FitzHugh Nagumo model) which study and report chimera states for φ values away from 0 or 2π .^{29,30} Although there is a slight dependence on the coupling range R , as both indices Z and $\Delta\omega$ indicate, this dependence is not very strong. Comparing the two maps, the $\Delta\omega$ one (Fig. 2b) shows higher details in the structure and higher ramifications in the frequency distributions.

Our numerical investigations demonstrate that interesting chimera states are produced when the values of the coherence indices escape the $(Z, \Delta\omega) \sim (1, 0)$ values. In particular, at the borderlines between the yellow (black-grey) and the dark regions (red-green) in Fig. 2a (b), one may observe the formation of stripe chimeras, several examples of which are provided in Fig. 3. In this figure, where $\varphi \approx 90^\circ$ and different values of R are used, alternation of coherent and incoherent stripes is recorded. Judging from the color-coded maps, Figs. 2a,b, we note that these chimera patterns are displayed for borderline parameter values, where $\Delta\omega$ just exceeds 0 and Z just falls below 1. In Figs. 3a and c two synchronous and 2 asynchronous stripes develop, while in panels b and d only one synchronous and one asynchronous stripe are recorded. It is worth to note that in Fig. 3a, b, c the stripes develop horizontally, while in d the stripes are vertical. This is due to the evolution of the random initial conditions, which are common in all simulations. Other pairs with notable stripe chimeras are recorded for (φ, R) values such as $(91^\circ, 8)$, $(92^\circ, 9)$, $(92^\circ, 10)$, $(94^\circ, 14)$, $(94^\circ, 15)$, $(95^\circ, 15)$, $(96^\circ, 15)$, $(95^\circ, 16)$, $(96^\circ, 16)$, $(95^\circ, 17)$, $(96^\circ, 17)$ and others.

One significant difference can be stressed between images in Fig. 1 (Turing patterns) and those in Fig. 3 (chimera states) and the ones that follow. In Fig. 1 the images are stationary

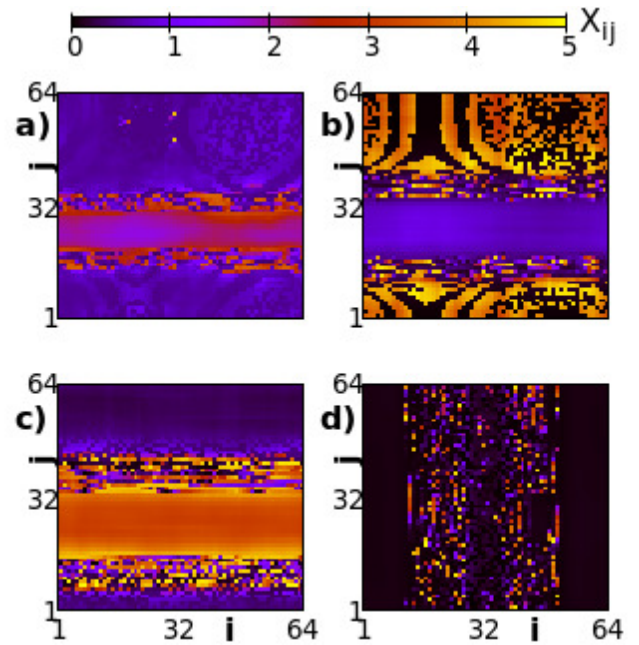


FIG. 3. Synchronous and asynchronous stripes for low φ -values. Spatial X -profiles for: a) $(\varphi = 91^\circ, R = 9)$, b) $(\varphi = 93^\circ, R = 14)$, c) $(\varphi = 96^\circ, R = 18)$ and d) $(\varphi = 97^\circ, R = 19)$. Other parameters are $A = 1.0$, $B = 2.9$, $dt = 0.010$, $D_X = D_Y = 1$, $N = 64$ and $\sigma = 1$. Toroidal periodic boundary conditions are applied. The images are recorded at 1000 TU. All simulations start from the same random initial conditions. A related video is presented in the Supplementary Material (Multimedia view corresponding to image Fig. 3c (movie_fig03c_brusselator_sig_1.00_phi_096_R_18.mp4)).

(still) after transient and do not change with time, while in Fig. 3 (and later on) the images are dynamic: the colors (state variables) oscillate in time, but the synchronous areas remain synchronous and so do the asynchronous ones. This means that in the color-coded spacetime plots in Fig. 3, the colors of all nodes (pixels) change continuously between black and yellow. To the contrary, in Fig. 1 they remain fixed after an initial transient period.

Stripes are also recorded when the high values of $\Delta\omega$ (low values of Z) cross to lower values of $\Delta\omega$ (high values of Z); this takes place around $\varphi \approx 300^\circ$, for different R -values. Spatial portraits of typical stripe chimeras in these parameter region are reported in Fig. 4. Panel a shows coexistence of a coherent (blue) and an incoherent stripe. In panel b, the coherent stripe has variable width. Such states are often unstable and they result in a turbulent incoherent state. Panels c (horizontal stripes) and d (vertical stripes) are stable chimeras, recorded for higher R values. Other parameter values producing interesting stripe chimeras in this area are the pairs (φ, R) : $(300^\circ, 14)$, $(299^\circ, 15)$, $(295^\circ, 16)$, $(298^\circ, 19)$, $(299^\circ, 19)$, $(296^\circ, 20)$, $(297^\circ, 20)$, $(298^\circ, 20)$ and $(299^\circ, 20)$.

We can also observe transitions from coherent traveling linear fronts to traveling chimera cores via the production of solitary states for rotation angle values around $\varphi \approx 220^\circ - 240^\circ$, in the center of the parameter regions of Fig. 2. In this param-

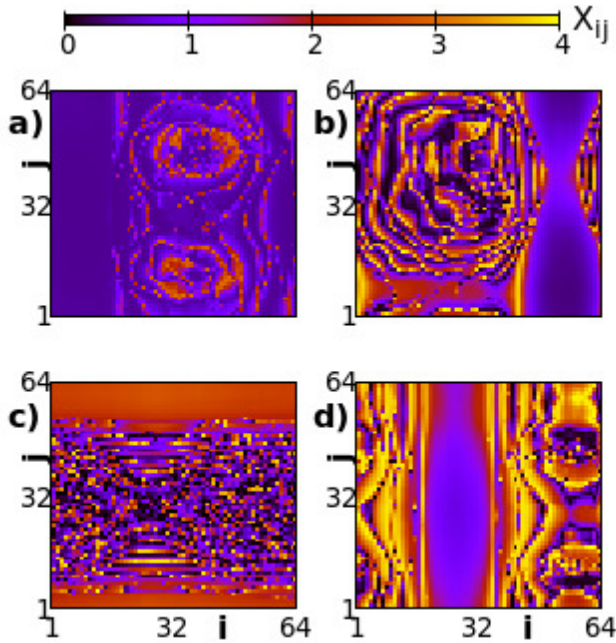


FIG. 4. Synchronous and asynchronous stripes for high φ -values. Spatial X -profiles for: a) ($\varphi = 298^\circ$, $R = 15$), b) ($\varphi = 299^\circ$, $R = 14$), c) ($\varphi = 295^\circ$, $R = 20$) and d) ($\varphi = 300^\circ$, $R = 19$). Other parameters as in Fig. 2. All simulations start from the same random initial conditions. A related video is presented in the Supplementary Material (Multimedia view corresponding to image Fig. 4c (movie_fig04c_brusselator_sig_1.00_phi_295_R_20.mp4)).

eter region $Z < 1$ and $\Delta\omega > 0$. Keeping $R = 21$, we gradually increase φ and we present the transitions from traveling coherent fronts to traveling coherent/incoherent domains, in Fig. 4. In this figure, the spatial X -profiles for $\varphi = 220^\circ$, $R = 21$ in panel a show the development of coherent traveling fronts. As the rotation coupling increases to $\varphi = 225^\circ$ we note in panel b the presence of a few (three) solitary Brusselators whose state variables escape from those of the neighbors. When φ is further increased to $\varphi = 228^\circ$, more solitaries mobilize causing perturbations in the linear structure of the traveling fronts, see panel c. For $\varphi = 229^\circ$ the solitaries organize into incoherent regions as shown in panel d. Further increase of φ to $\varphi = 236^\circ$ causes increase in the size of the incoherent regions and total deformation of the linear structure of the traveling fronts. Finally, for $\varphi = 236^\circ$ the coherent fronts break totally and incoherent cores are formed as satellites to traveling coherent domains. Indeed, one can observe ramifications in the $\Delta\omega$ values in the central part of Fig. 2b, which justify the presence of traveling front (coherent structures) with $\Delta\omega = 0$ (black regions) next to traveling chimera states with $\Delta\omega > 0$ (red and blue regions). Similar behavior involving transitions from coherent traveling fronts to moving chimera states via solitary mobilization is observed for large and intermediate values of R and intermediate φ domains.

In the vicinity of $\varphi \approx \pi (= 180^\circ)$ we can observe multiple coherent spots surrounded by an incoherent halos. Depending on the parameter value, the size and number of the co-

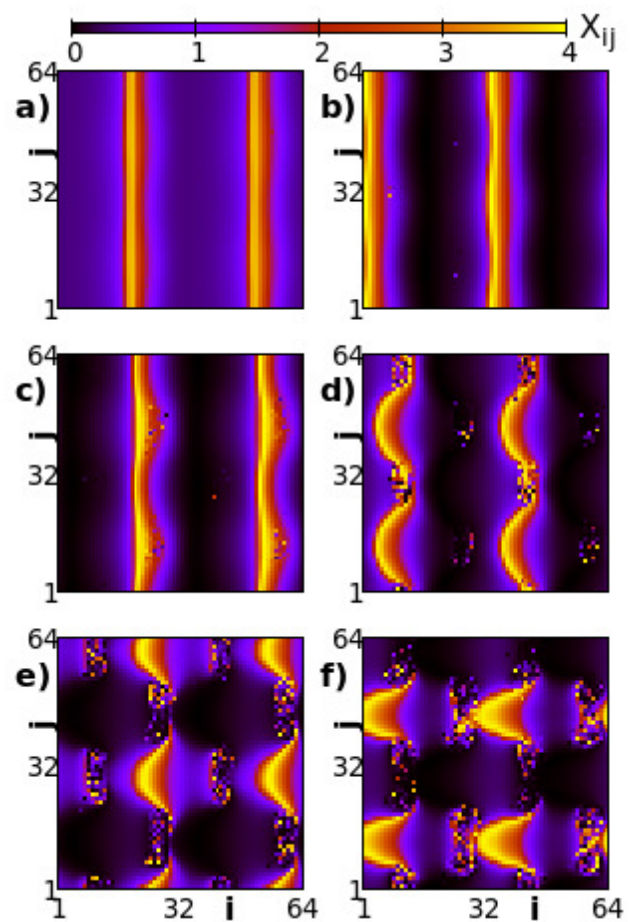


FIG. 5. Transitions from coherent stripes to solitaries and further to coherent and incoherent traveling domains. Spatial X -profiles for: a) ($\varphi = 220^\circ$, $R = 21$), b) ($\varphi = 225^\circ$, $R = 21$), c) ($\varphi = 228^\circ$, $R = 21$), d) ($\varphi = 229^\circ$, $R = 21$), e) ($\varphi = 230^\circ$, $R = 21$) and f) ($\varphi = 236^\circ$, $R = 21$). Other parameters as in Fig. 2. All simulations start from the same random initial conditions. A related video is presented in the Supplementary Material (Multimedia view corresponding to image Fig. 5e (movie_fig05e_brusselator_sig_1.00_phi_230_R_21.mp4)).

herent spots varies to cover exhaustively the 2D lattice. Representative examples are provided in Fig. 6. In panel a, for $\varphi = 160^\circ$, $R = 16$, three zones of interconnected coherent spots are observed. These zones are separated by coherent ones of varying width. The borders between the coherent spots and the coherent zones consist of incoherent elements. The coherent spots and coherent zones are characterized by a small, but persistent phase difference. When the connectivity range increases to $R = 21$ in panel b, the number (and form) of the coherent spots decreases (from 9 to 4) and the area of the incoherent domains grows. The coherent strings also degenerate into 4 coherent domains lagging behind with respect to the value of the state variable as compared to the coherent spots. In panel c, for different parameter values (in the same parameter domain) $\varphi = 165^\circ$, $R = 19$, the size of the connected coherent spots increases and their multiplicity de-

creases to 4. Here the phase difference between the coherent spots and the coherent zones is considerable, the former being in the red-yellow colors (highest X -values), while the latter are in the black-blue colors (lowest X -values). By increasing slightly φ to 166° , in panel d, the phase difference between the coherent spots and the coherent zones vanishes and the connecting incoherent domains are now visible in vivid colors.

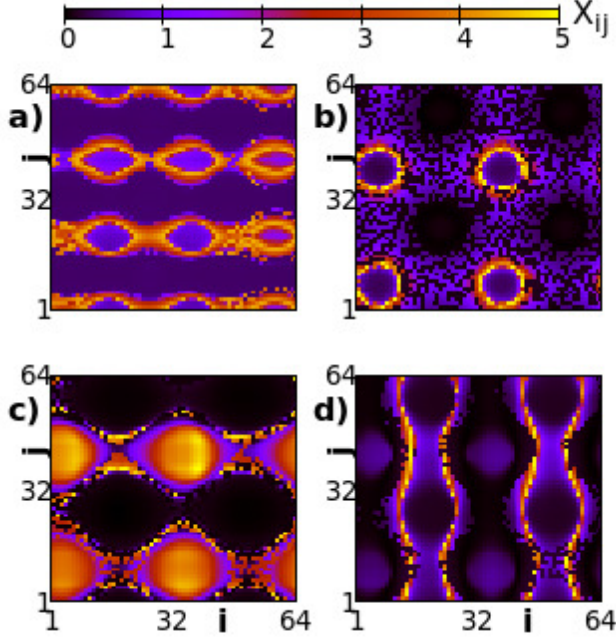


FIG. 6. Multiple connected and disconnected coherent spots. Spatial 2D X -profiles for: a) ($\varphi = 160^\circ$, $R = 16$), b) ($\varphi = 160^\circ$, $R = 21$), c) ($\varphi = 165^\circ$, $R = 19$) and d) ($\varphi = 166^\circ$, $R = 19$). Other parameters as in Fig. 2. All simulations start from the same random initial conditions.

Along the right border between turbulent states and coherence, stable incoherent spots may develop for appropriate values of the system parameters. These can be considered as shrinking or degeneration of the stripes which are observed in nearby parameter areas (see Fig. 4). In Fig. 7 a variety of incoherent spots are recorded, for parameter values $302 \leq \varphi \leq 304$ and different R .

Besides the patterns discussed above, we also report the following ones:

- For $\varphi \approx 170^\circ - 200^\circ$, traveling square coherent domains develop. Depending on the values of R the coherent squares can be surrounded by incoherent halos.
- Linear coherent stripes cross the system for large values of R , e.g., $R = 21$ and $203^\circ \leq \varphi \leq 225^\circ$ and other parameters values in the same area.
- Combinations of coherent linear parts and incoherent irregular shapes are often recorded. These are observed for smaller values of R , e.g., $R = 6$ and similar values.

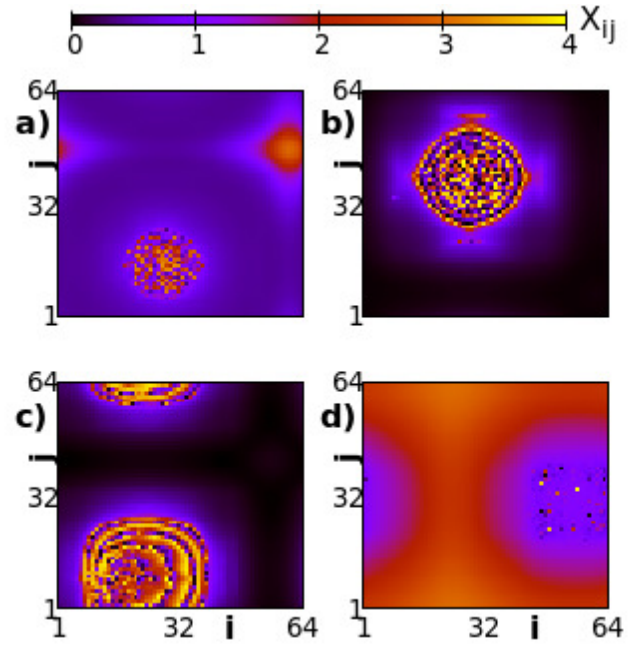


FIG. 7. Single incoherent spots. Spatial 2D X -profiles for: a) ($\varphi = 303^\circ$, $R = 6$), b) ($\varphi = 302^\circ$, $R = 10$), c) ($\varphi = 304^\circ$, $R = 8$) and d) ($\varphi = 302^\circ$, $R = 18$). Other parameters as in Fig. 2. All simulations start from the same random initial conditions. Two related videos are presented in the Supplementary Material (Multimedia view corresponding to image Fig. 7b (movie_fig07b_brusselator_sig_1.00_phi_302_R_10.mp4) and Fig. 7c (movie_fig07c_brusselator_sig_1.00_phi_304_R_08.mp4)).

- Scroll waves are recorded for parameter values near the stable chimera patterns, when the incoherent domains dissolve, e.g., for $\varphi \approx 300^\circ$ and $2 \leq R \leq 10$. Examples of these and other turbulent chimera patterns are shown in Appendix B.
- Results for the case $R = 1$, which corresponds to the diffusion limit, are also shown in Appendix B.

The parameter domain where the various patterns dominate were obtained for the working parameter set given in the first paragraph of the present section. For different generic parameter values the borders between the various domains of coherence are adjusted appropriately.

V. GENERAL COMMENTS ON SPATIAL AND SPATIOTEMPORAL PATTERN FORMATION IN THE BRUSSELTOR MODEL

From the results in the previous two sections, it becomes clear that in different parameter domains the Brusselator network exhibits different spatial (Turing) and spatiotemporal (chimera) patterns of high complexity.

Indeed, Turing patterns described in section III are spatial patterns which are stable in time after a transient period, while in chimera states all elements perform nonlinear oscillations,

but they are spatially organized in coherent and incoherent domains. As an additional evidence of the intrinsic difference in the temporal evolution between these two types of patterns, we present in the two figures below the temporal evolution of particular oscillators, in Fig. 8, and their corresponding Fourier spectra, in Fig. 9. We have chosen to demonstrate this for parameters as in Fig. 1a1 corresponding to the Turing regime and Fig. 4c in the chimera regime.

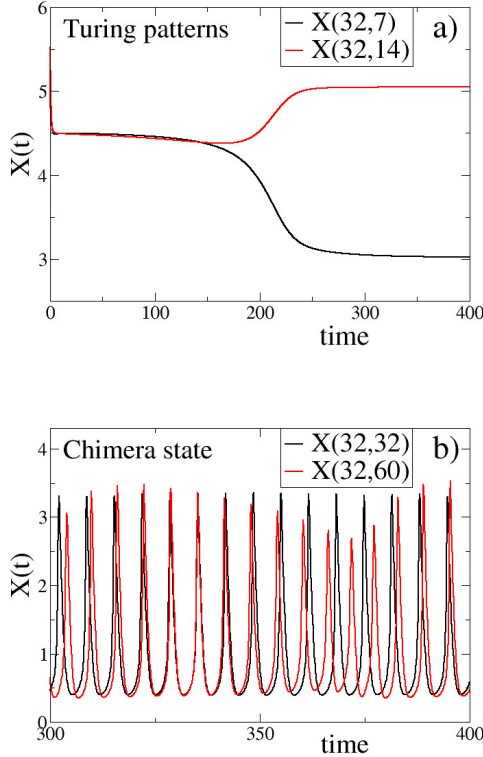


FIG. 8. Temporal evolution of Brusselator elements: a) For parameter values in the Turing regime, as in Fig. 1a1. The black solid (lower) line corresponds to the element (32,7) in the center of a spot and the red (upper) line to the element (32,14) outside the spot areas. Other parameters as in Fig. 1a1. b) For parameter values in the chimera regime, as in Fig. 4c. The red solid line corresponds to the element (32,60) in the coherent region and the black line to the element (32,32) in the incoherent stripe. Other parameters as in Fig. 4c.

From Fig. 8a, it is evident that the Brusselators with parameters set at the Turing regime reach a stable steady state, different for each element. Namely, the X -variable of Brusselator at position (32,7), which corresponds to the center of a spot in Fig. 1a1, reaches value $X(32,7) \rightarrow \sim 3$, while the one at position (32,14), which is located outside the spot areas, reaches $X(32,14) \rightarrow \sim 5$. To the contrary, when the Brusselators are set in the chimera regime, they all oscillate in time, as shown in Fig. 8b. In Fig. 8b (red line), we have chosen to demonstrate the temporal evolution of a node in the coherent domain, (node (32,60) in Fig. 4c). In the same figure the black line shows the evolution of a node in the incoherent domain

(node (32,32) in Fig. 4c). Both elements show similar oscillations, however, we may observe that the Brusselator which belongs to the incoherent region, position (32,32), is characterized by lower frequency of oscillations than the one at position (32,60) in the coherent region. This is a well known property of chimera states, where the coherent and incoherent regions are characterized by different frequencies^{22,30,69,72}, as will be also verified in the next figure. Similar results and conclusions are obtained for all other parameters in the chimera regime.

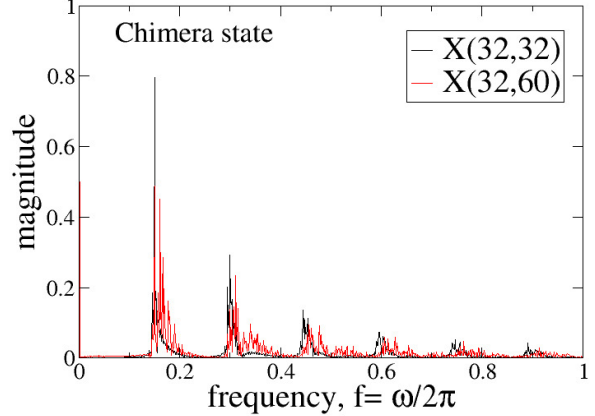


FIG. 9. Fourier spectra corresponding to the temporal evolution of the Brusselator elements shown in Fig. 8b. The parameter values and line descriptions follow the ones in Fig. 8b. For the extraction of the Fourier spectra DFT Fourier transform was used and time series covered approximately approximately 170 cycles, in both cases, excluding the first 50 cycles as transient.

To investigate the difference in the frequencies in the coherent and incoherent domains of the chimera states, as an example we plot in Fig. 9 the Fourier spectra of the two time series shown in Fig. 8b. We choose again the same two Brusselator elements at positions (32,60), in the coherent region, plotted with the red line and at position (32,32), in the incoherent region, plotted with black line. From the plot, it is evident that for both elements only one frequency prevails, together with the corresponding harmonics. The maxima in the two curves are at different positions, consistently for the main frequencies and their harmonics. This observation corroborates the statement in the previous paragraph on the difference in the oscillator frequencies in the coherent and the incoherent regions of the chimera states.

VI. CONCLUSIONS

We have investigated the conditions under which Turing patterns and chimera states can be produced in the same non-linear dynamical system. Using as exemplary case the Brusselator model, we have demonstrated Turing patterns for parameter regions where the single node dynamics presents fixed

points. The same dynamical system exhibits chimera states if the parameters of the single element are chosen in the oscillatory (limit cycle) regime. Connectivity-wise, for the emergence of the Turing patterns small connectivity neighborhoods are required, mimicking the nearest neighbor, Laplacian diffusion, while for the production of chimera states the connectivity regions need to be of intermediate range.

Based on the above results and discussions, we may add that it is not possible to obtain chimera states and Turing patterns for the same values of parameters A and B in the Brusselator model, even if the other (connectivity) parameters are different. This is because for the emergence of Turing patterns (stable steady states) the single element dynamics need to lead to fixed points, while for the emergence of chimera states (oscillatory steady states) a limit cycle is necessary in the single element dynamics. The above conclusions hold provided that the coupling terms do not drastically alter the nodal dynamics. Additional numerical and analytical studies using different coupled nonlinear models are necessary to further elucidate the necessary and sufficient conditions for the presence of chimera states in these systems.

ACKNOWLEDGMENTS

The author (A.P.) acknowledges helpful discussions with K. Anesiadis. This work was supported by computational time granted from the Greek Research & Technology Network (GRNET) in the National HPC facility - ARIS, under project

IDs PR009012 and PR12015.

DATA AVAILABILITY STATEMENT

The data that support the findings of this study are available from the corresponding author upon reasonable request.

Appendix A: Discrete form of Brusselator with diffusion

In this appendix we discretize the Brusselator model with diffusion and bring it to the general form, Eq. (4), in order to use a generic system of differential equations, both for the production of Turing patterns and chimera states (at different regions of the parameter space).

Starting from Eq. (10), we specify the location (i, j) of a Brusselator node and analyze the Laplacian operator around this location. Then, Eq. (10) reduces to:

$$\frac{dX_{ij}}{dt} = A - (B + 1)X_{ij} + X_{ij}^2 Y_{ij} + D_X \nabla^2 X_{ij} \quad (\text{A1a})$$

$$\frac{dY_{ij}}{dt} = BX_{ij} - X_{ij}^2 Y_{ij} + D_Y \nabla^2 Y_{ij}. \quad (\text{A1b})$$

where ∇^2 is the Laplacian operator in two dimensions and D_X, D_Y are the diffusion constants of the X and Y variables, respectively. By expanding the Laplacian operator in space around position (i, j) we obtain:

$$\frac{dX_{ij}}{dt} = A - (B + 1)X_{ij} + X_{ij}^2 Y_{ij} + \frac{D_X}{(\Delta x)^2} [X_{i+1,j} - 2X_{ij} + X_{i-1,j}] + \frac{D_X}{(\Delta y)^2} [X_{i,j+1} - 2X_{ij} + X_{i,j-1}] \quad (\text{A2a})$$

$$\frac{dY_{ij}}{dt} = BX_{ij} - X_{ij}^2 Y_{ij} + \frac{D_Y}{(\Delta x)^2} [Y_{i+1,j} - 2Y_{ij} + Y_{i-1,j}] + \frac{D_Y}{(\Delta y)^2} [Y_{i,j+1} - 2Y_{ij} + Y_{i,j-1}]. \quad (\text{A2b})$$

In Eqs. (A2), Δx and Δy represent the infinitesimal displacement on the x - and y -axis, respectively, as per the derivative definition. In the case of discretization, the smallest possible displacement on the lattice is one lattice site, and therefore $\Delta x = \Delta y = h = 1$ in the network discretization approximation.

Seeing from a different point of view, the displacement values Δx and Δy can be absorbed in the factor D_X and D_Y . Gathering together the terms which are linked to the neighboring nodes, Eq. (A2) reduce further to:

$$\frac{dX_{ij}}{dt} = A - (B + 1)X_{ij} + X_{ij}^2 Y_{ij} + \frac{D_X}{(\Delta x)^2} \sum_{k=i-1}^{i+1} [X_{kj} - X_{ij}] + \frac{D_X}{(\Delta y)^2} \sum_{l=j-1}^{j+1} [X_{il} - X_{ij}] \quad (\text{A3a})$$

$$\frac{dY_{ij}}{dt} = BX_{ij} - X_{ij}^2 Y_{ij} + \frac{D_Y}{(\Delta x)^2} \sum_{k=i-1}^{i+1} [Y_{kj} - Y_{ij}] + \frac{D_Y}{(\Delta y)^2} \sum_{l=j-1}^{j+1} [Y_{il} - Y_{ij}]. \quad (\text{A3b})$$

Finally, gathering the terms on the right-hand-sides and because $\Delta x = \Delta y = h = 1$, Eqs. (A3) result in:

$$\frac{dX_{ij}}{dt} = A - (B+1)X_{ij} + X_{ij}^2 Y_{ij} + \frac{D_X}{h^2} \sum_{\{k,l\}} [X_{kl} - X_{ij}] \quad (\text{A4a})$$

$$\frac{dY_{ij}}{dt} = BX_{ij} - X_{ij}^2 Y_{ij} + \frac{D_Y}{h^2} \sum_{\{k,l\}} [Y_{kl} - Y_{ij}]. \quad (\text{A4b})$$

Equations (A4) have the same form with the more general Eqs. (4), with the following restrictions:

$$c_{ij;kl} w_{XX} = D_X/h^2, \quad (\text{A5a})$$

$$c_{ij;kl} w_{YY} = D_Y/h^2, \quad (\text{A5b})$$

$$w_{XY} = w_{YX} = 0, \quad (\text{A5c})$$

$$R = 1. \quad (\text{A5d})$$

I.e., the more generic form of the Brusselator network, Eqs. (4), can give rise to Turing patterns when cross-coupling terms are absent from the dynamics and in the limit of local, nearest-neighbor exchanges, i.e., under the conditions Eqs. (A5).

Appendix B: Additional turbulent chimeric patterns

In the present section additional interesting patterns are recorded, composed by coexisting coherent and incoherent traveling patterns.

First, in Fig. 10 turbulent traveling patterns are shown. Of particular interest is panel d, which consists of traveling fronts (red colors). One of the fronts forms a spiral pattern at the interior of which an incoherent core dominates. Similar incoherent cores are reported in Refs.^{77,78} where the ZBKE model is used.

Of special interest are the patterns developed for $R = 1$ and with various φ values. Note that the case $R = 1$ does not strictly correspond to the discretized regular diffusion, due to the influence of the rotational matrix φ . Only the case $\varphi = 0$, $R = 1$ can be considered as regular diffusion. The results for incremental values of φ are shown in Fig. 11a-h.

For small $\varphi \leq 73^\circ$ and large $\varphi \geq 314^\circ$ values of the rotation angle, the system presents coherence as shown in Fig. 11a and h. Between these values a certain degree of incoherence reins in the system as presented in panels b to g of the same figure. The borderline values written here were obtained for the working parameter set given in the first paragraph of section IV. For different generic parameter values the borders between full coherence and partial coherence (chimera states) are appropriately adjusted.

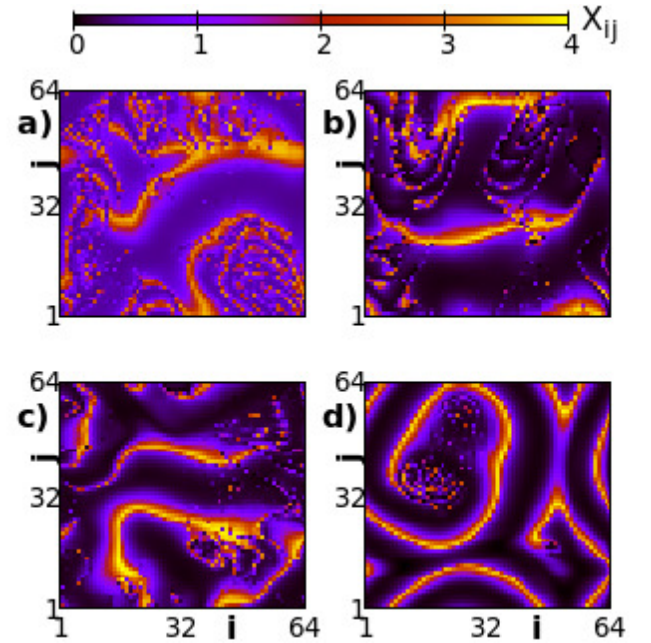


FIG. 10. Turbulent patterns. Spatial 2D X -profiles for: a) ($\varphi = 303^\circ$, $R = 6$), b) ($\varphi = 302^\circ$, $R = 10$), c) ($\varphi = 304^\circ$, $R = 8$) and d) ($\varphi = 302^\circ$, $R = 18$). Other parameters as in Fig. 2. All simulations start from the same random initial conditions.

Finally, a notable stable pattern was recorded in the vicinity of the parameter regions where the coherent stripes were found, for $87^\circ \leq \varphi \leq 92^\circ$ and $5 \leq R \leq 12$. An example is provided in Fig. 12 for ($\varphi = 91^\circ$, $R = 10$); it consists of two asymmetric coherent spots. The asymmetric spots oscillate out of phase, as one can see from the present snapshot where at the same time the X -variable of the largest spot is ≈ 0.5 (blue color) and $X \approx 3$ (orange color) for the smaller one. Traces of similar patterns are also seen in the surroundings of this parameter value.

¹I. Epstein and J. Pojman, *An introduction to nonlinear chemical dynamics* (Oxford University Press, Oxford, 1998).

²A. Turing, *Philosophical Transactions of the Royal Society B* **237**, 37 (1952).

³G. Nicolis and I. Prigogine, *Self-organization in nonequilibrium systems* (Wiley, New York, 1977).

⁴R. Lefever and G. Nicolis, *Journal of Theoretical Biology* **30**, 267 (1971).

⁵G. Nicolis, *Introduction to Nonlinear Science* (Cambridge University Press, Cambridge, 1995).

⁶I. Epstein and K. Showalter, *Journal of Physical Chemistry* **100**, 13132 (1996).

⁷A. Mikhailov and K. Showalter, *Physics Reports* **425**, 79 (2006).

⁸A. T. Winfree, *Progress in Theoretical Chemistry* **4**, 1 (1978).

⁹P. D. Kepper, V. Castets, E. Dulos, and J. Boissonade, *Physica D* **49**, 161 (1991).

¹⁰V. Castets, E. Dulos, J. Boissonade, and P. D. Kepper, *Physical Review Letters* **64**, 2953 (1990).

¹¹P. Borckmans, G. Dewel, D. Walgraef, and Y. Katayama, *Journal of Statistical Physics* **48**, 1031 (1987).

¹²J. Verdasca, A. D. Wit, G. Dewel, and P. Borckmans, *Physics Letters A* **168**, 194 (1992).

¹³P. Borckmans, A. D. Wit, and G. Dewel, *Physica A* **188**, 137 (1992).

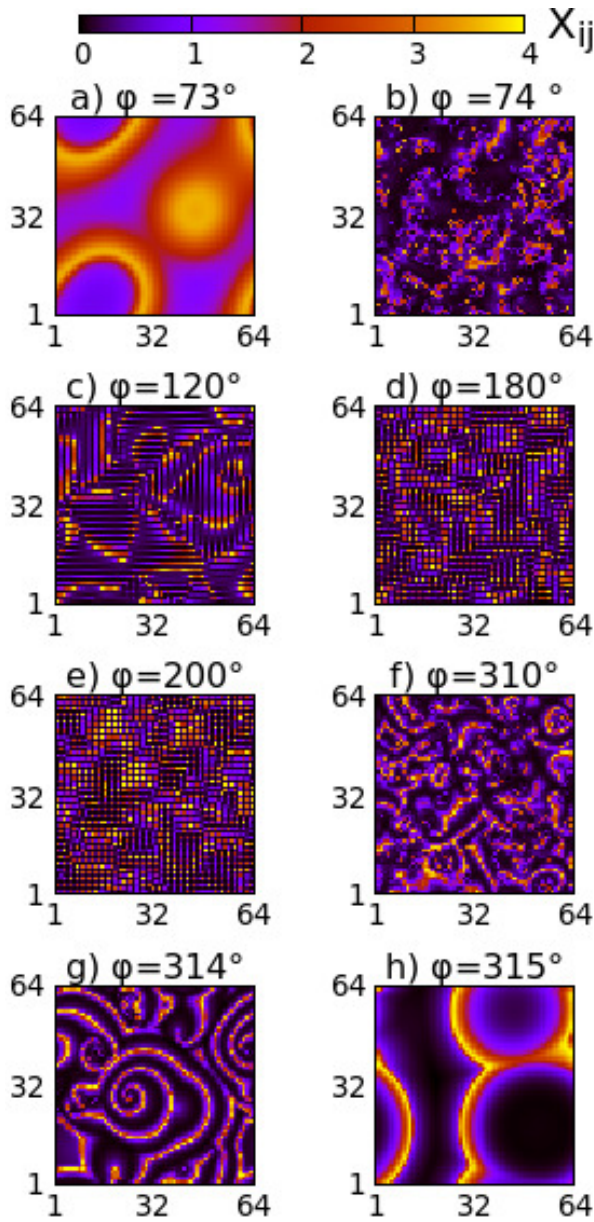


FIG. 11. Spatiotemporal patterns for $R = 1$. Spatial 2D X -profiles for: a) $\varphi = 73^\circ$, b) $\varphi = 74^\circ$, c) $\varphi = 120^\circ$, d) $\varphi = 180^\circ$, e) $\varphi = 200^\circ$, f) $\varphi = 310^\circ$, g) $\varphi = 314^\circ$ and h) $\varphi = 315^\circ$. The x-axis correspond to the horizontal arrangement of the Brusselators and the y-axis to their vertical arrangement on the 2D square lattice network. Other parameters as in Fig. 2. All simulations start from the same random initial conditions.

¹⁴B. Pena and C. Perez-Garcia, *Physical Review E* **64**, 056213 (2001).

¹⁵R. J. Field, E. Koros, and R. M. Noyes, *Journal of the American Chemical Society* **94**, 8649 (1972).

¹⁶R. J. Field and R. M. Noyes, *Journal of Chemical Physics* **60**, 1877 (1974).

¹⁷P. K. Becker and R. J. Field, *Journal of Chemical Physics* **89**, 118 (1985).

¹⁸I. Berenstein, D. Bullara, and Y. D. Decker, *Chaos* **24**, 033129 (2014).

¹⁹M. Hildebrand, A. Sködt, and K. Showalter, *Physical Review Letters* **87**, 088303 (2001).

²⁰A. M. Zhabotinsky, F. Buchholtz, A. B. Kiyatkin, and I. R. Epstein, *Journal of Physical Chemistry* **97**, 75 (1993).

²¹S. Nkomo, M. R. Tinsley, and K. Showalter, *Physical Review Letters* **110**,

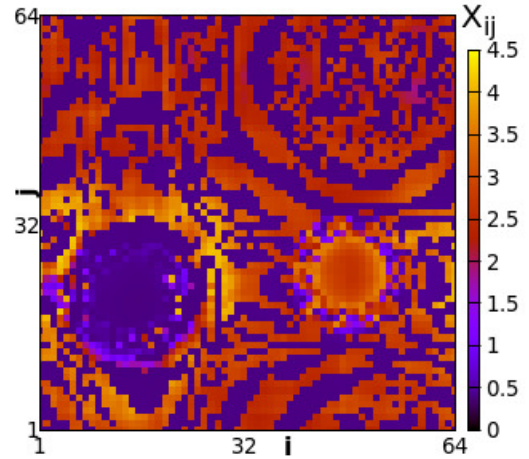


FIG. 12. Spatial 2D X -profiles for the two asymmetric stable coherent spots occurring at: ($\varphi = 91^\circ$, $R = 10$). Other parameters as in Fig. 2. All simulations start from the same random initial conditions.

244102 (2013).

²²Y. Kuramoto and D. Battogtokh, *Nonlinear Phenomena in Complex Systems* **5**, 380 (2002).

²³Y. Kuramoto, in *Nonlinear Dynamics and Chaos: Where do we go from here?*, edited by S. J. Hogan, A. R. Champneys, A. R. Krauskopf, M. di Bernardo, R. E. Wilson, H. M. Osinga, and M. E. Homer (CRC Press, 2002) pp. 209–227.

²⁴D. M. Abrams and S. H. Strogatz, *Physical Review Letters* **93**, 174102 (2004).

²⁵M. I. Bolotov, G. V. Osipov, and A. Pikovsky, *Physical Review E* **93**, 032202 (2016).

²⁶R. J. Goldschmidt, A. Pikovsky, and A. Politi, *Chaos* **29**, 071101 (2019).

²⁷M. I. Bolotov, L. A. Smirnov, G. V. Osipov, and A. Pikovsky, *Physical Review E* **102**, 042218 (2020).

²⁸H. Sakaguchi, *Physical Review E* **73**, 031907 (2006).

²⁹I. Omelchenko, O. E. Omel'chenko, P. Hövel, and E. Schöll, *Physical Review Letters* **110**, 224101 (2013).

³⁰I. Omelchenko, A. Provata, J. Hizanidis, E. Schöll, and P. Hövel, *Physical Review E* **91**, 022917 (2015).

³¹A. Schmidt, T. Kasimatis, J. Hizanidis, A. Provata, and P. Hövel, *Physical Review E* **95**, 032224 (2017).

³²A. Zakharova, N. Semenova, V. S. Anishchenko, and E. Schöll, *Chaos* **27**, 114320 (2017).

³³I. A. Shepelev and T. E. Vadivasova, *Communications in Nonlinear Science and Numerical Simulation* **79**, 104925 (2019).

³⁴J. Hizanidis, V. Kanas, A. Bezerianos, and T. Bountis, *International Journal of Bifurcations and Chaos* **24**, 1450030 (2014).

³⁵S. Ulonska, I. Omelchenko, A. Zakharova, and E. Schöll, *Chaos* **26**, 094825 (2016).

³⁶A. Yeldesbay, A. Pikovsky, and M. Rosenblum, *Physical Review Letters* **112**, 144103 (2014).

³⁷A. Gjurchinovski, E. Schöll, and A. Zakharova, *Physical Review E* **95**, 042218 (2017).

³⁸L. Tumash, E. Panteley, A. Zakharova, and E. Schöll, *European Physical Journal B* **92**, 100 (2018).

³⁹S. Olmi, E. A. Martens, S. Thutupalli, and A. Torcini, *Physical Review E* **92**, 030901 (2015).

⁴⁰N. D. Tsigkri-DeSmedt, J. Hizanidis, E. Schöll, P. Hövel, and A. Provata, *The European Physical Journal B* **90**, 139 (2017).

⁴¹N. D. Tsigkri-DeSmedt, I. Koulterakis, G. Karakos, and A. Provata, *The European Physical Journal B* **91**, 305 (2018).

⁴²V. Maistrenko, O. Sudakov, O. Osiv, and Y. Maistrenko, *European Physical*

- Journal: Special Topics **226**, 1867 (2017).
- ⁴³C. R. Laing, *SIAM Journal on Applied Dynamical Systems* **16**, 974 (2017).
- ⁴⁴O. E. Omel'Chenko and E. Knobloch, *New Journal of Physics* **21**, 093034 (2019).
- ⁴⁵Y. Maistrenko, O. Sudakov, O. Osiv, and V. Maistrenko, *New Journal of Physics* **17**, 073037 (2015).
- ⁴⁶T. Kasimatis, J. Hizanidis, and A. Provata, *Physical Review E* **97**, 052213 (2018).
- ⁴⁷V. Maistrenko, O. Sudakov, and O. Osiv, *Chaos* **30**, 063113 (2020).
- ⁴⁸I. Koulrierakis, D. A. Verganelakis, I. Omelchenko, A. Zakharova, E. Schöll, and A. Provata, *Chaos* **30**, 113137 (2020).
- ⁴⁹A. M. Hagerstrom, T. E. Murphy, R. Roy, P. Hövel, I. Omelchenko, and E. Schöll, *Nature Physics* **8**, 658 (2012).
- ⁵⁰L. V. Gambuzza, A. Buscarino, S. Chessari, L. Fortuna, R. Meucci, and M. Frasca, *Physical Review E* **90**, 032905 (2014).
- ⁵¹E. A. Martens, S. Thutupalli, A. Fourrière, and O. Hallatschek, *Proceedings of the National Academy of Sciences* **110**, 10563 (2013).
- ⁵²T. Kapitaniak and J. Kurths, *European Physical Journal: Special Topics* **223**, 609 (2014).
- ⁵³D. Dudkowski, J. Grabski, J. Wojewoda, P. Perlikowski, Y. Maistrenko, and T. Kapitaniak, *Scientific Reports* **6**, 29833 (2016).
- ⁵⁴K. Manoj, S. A. Pawar, and R. I. Sujith, *Physical Review E* **103**, 022207 (2021).
- ⁵⁵E. M. Cherry and F. H. Fenton, *New Journal of Physics* **10**, 125016 (2008).
- ⁵⁶F. Mormann, K. Lehnertz, P. David, and C. E. Elger, *Physica D* **144**, 358 (2000).
- ⁵⁷F. Mormann, T. Kreuz, R. G. Andrzejak, P. David, K. Lehnertz, and C. E. Elger, *Epilepsy Res.* **53**, 173 (2003).
- ⁵⁸M. S. Santos, J. D. Szezech, F. S. Borges, K. C. Iarosz, I. L. Caldas, A. M. Batista, R. L. Viana, and J. Kurths, *Chaos, Solitons & Fractals* **101**, 86 (2017).
- ⁵⁹M. R. Tinsley, S. Nkomo, and K. Showalter, *Nature Physics* **8**, 662 (2012).
- ⁶⁰M. Wickramasinghe and I. Z. Kiss, *PLoS ONE* **8** (2013).
- ⁶¹L. Schmidt, K. Schönleber, K. Krischer, and V. García-Morales, *Chaos* **24**, 013102 (2014).
- ⁶²N. C. Rattenborg, C. J. Amlaner, and S. L. Lima, *Neuroscience and Biobehavioral Reviews* **24**, 817 (2000).
- ⁶³N. C. Rattenborg, *Naturwissenschaften* **93**, 413 (2006).
- ⁶⁴L. Ramlow, J. Sawicki, A. Zakharova, J. Hlinka, J. C. Claussen, and E. Schöll, *Europhysics Letters* **126**, 50007 (2019).
- ⁶⁵R. G. Andrzejak, C. Rummel, F. Mormann, and K. Schindler, *Scientific Reports* **6**, 23000 (2016).
- ⁶⁶G. Ruzzene, I. Omelchenko, E. Schöll, A. Zakharova, and R. G. Andrzejak, *Chaos* **29**, 0511031 (2019).
- ⁶⁷K. Bansal, J. O. Garcia, S. H. Tompson, T. Verstynen, J. M. Vettel, and S. F. Muldoon, *Science Advances* **5**, eaau853 (2019).
- ⁶⁸M. J. Panaggio and D. Abrams, *Nonlinearity* **28**, R67 (2015).
- ⁶⁹E. Schöll, *European Physical Journal – Special Topics* **225**, 891 (2016).
- ⁷⁰N. Yao and Z. Zheng, *International Journal of Modern Physics B* **30**, 1630002 (2016).
- ⁷¹S. Majhi, B. K. Bera, D. Ghosh, and M. Perc, *Physics of Life Reviews* **28**, 100 (2019).
- ⁷²O. E. Omel'Chenko, *Nonlinearity* **31**, R121 (2018).
- ⁷³A. Zakharova, *Chimera Patterns in Networks: Interplay between Dynamics, Structure, Noise, and Delay* (Understanding Complex Systems, Springer International Publishing, 2020).
- ⁷⁴O. E. Omel'Chenko, *Journal of Nonlinear Science* **32**, 22 (2022).
- ⁷⁵A. F. Tutz, M. R. Tinsley, and K. Showalter, *Physical Chemistry Chemical Physics* **17**, 20047 (2015).
- ⁷⁶S. Nkomo, M. R. Tinsley, and K. Showalter, *Chaos* **26**, 094826 (2016).
- ⁷⁷J. F. Tutz, J. Rode, M. R. Tinsley, K. Showalter, and H. Engel, *Nature Physics* **14**, 282 (2018).
- ⁷⁸J. F. Tutz, M. R. Tinsley, H. Engel, and K. Showalter, *Scientific Reports* **10**, 7821 (2020).
- ⁷⁹J. Hizanidis, E. Panagakou, I. Omelchenko, E. Schöll, P. Hövel, and A. Provata, *Physical Review E* **92**, 012915 (2015).
- ⁸⁰I. Franović, O. E. Omel'Chenko, and M. Wolfrum, *Physical Review E* **104**, L052201 (2021).
- ⁸¹J. Hizanidis, N. Lazarides, and G. P. Tsironis, *Chaos* **30**, 013115 (2020).
- ⁸²T. Kokolnikov, T. Erneux, and J. Wei, *Physica D* **214**, 63 (2006).
- ⁸³M. A. Budroni and A. D. Wit, *Physical Review E* **93**, 062207 (2016).
- ⁸⁴D. Bullara, Y. D. Decker, and R. Lefever, *Physical Review E* **87**, 062023 (2013).
- ⁸⁵M. Tildi, Y. Gandica, G. Sonnino, E. Averlant, and K. Panajotov, *Entropy* **18**, 64 (2016).
- ⁸⁶H. Shoji, K. Yamada, D. Ueyama, and T. Ohta, *Physical Review E* **75**, 046212 (2007).
- ⁸⁷O. E. Omel'Chenko, M. Wolfrum, and Y. L. Maistrenko, *Physical Review E* **81**, 065201(R) (2010).
- ⁸⁸M. Mikhaylenko, L. Ramlow, S. Jalan, and A. Zakharova, *Chaos* **29**, 023122 (2019).
- ⁸⁹C. Bick, P. Ashwin, and A. Rodrigues, *Chaos* **26**, 094814 (2016).